An Improved Mesh-Free Approach for Electrical Impedance Tomography Using Modified Element-Free Galerkin Method and Neural Network Correction

Maedeh Hadinia[1], Amir Zare-Bazghaleh[2]*
[1] Assistant professor, Department of Physics and Medical Engineering, Ra.C., Islamic Azad University, Rasht, Iran, +989111853350, mhadinia@iau.ac.ir.
[2] Assistant professor, Department of Electrical Engineering, Lan.C., Islamic Azad University, Langarud, Iran, +989112947785, amirzarebazghaleh@iau.ac.ir
Receive Date: 16 June 2025 Revise Date: 07 July 2025 Accept Date: 21 July 2025

Abstract

Electrical Impedance Tomography (EIT) is a promising imaging modality whose accuracy strongly depends on the precision of its forward problem solution. In this study, a Modified Element-Free Galerkin Method (MEFG) is developed to solve both forward and inverse problems in EIT. The MEFG approach preserves the mesh-free advantages of the conventional Element-Free Galerkin(EFG) Methodwhile directly imposing essential boundary conditions through modified shape functions that satisfy the Kronecker delta property. To further improve reconstruction accuracy, a back-propagation neural network is trained to reduce discrepancies between simulated and exact data during inverse problem. Numerical experiments using a heterogeneous model demonstrate that MEFG achieves superior forward model accuracy compared to the traditional finite element method. Additionally, theMEFG improves image reconstruction stability in the presence of measurement noise, validating the robustness of the proposed approach for practical biomedical EIT applications.

Keywords: Electrical impedance tomography, Modified element-free Galerkin method, Mesh-free methods, Neural network, Image reconstruction

1. Introduction

Electrical Impedance Tomography (EIT) is a non-invasive imaging modality used in clinical and industrial applications to estimate internal conductivity distributions based on boundary voltage measurements acquired via surface electrodes [1- 16]. Solving the nonlinear, ill-posed inverse problem of EIT requires highly accurate solutions to the associated forward problem. The forward problem involves solving a boundary value problem derived from Maxwell's equations, typically approximated by Laplace's equation for isotropic, quasi-static media.

Numerical methods are widely employed to solve the EIT forward problem. Among them, Finite Element (FE)method is the most popular due to its flexibility in modeling complex domains; however, its reliance on mesh generation limits its efficiency for irregular and deformable geometries, such as heterogeneous biological tissues.

To address these challenges, mesh-free approaches like the Element-Free Galerkin (EFG) Methodhave been introduced [17, 18]. Unlike FE, EFG requires only scattered nodal data, eliminating the need for meshing and offering superior flexibility in dynamic or complex geometries. EFG has been successfully applied to EIT forward problems [19- 21]. Nevertheless, a major drawback is that its Moving Least Squares (MLS) shape

functions do not satisfy the Kronecker delta property, complicating the direct imposition of essential boundary conditions.

The Modified Element-Free Galerkin Method (MEFG) modifies MLS shape functions to satisfy the Kronecker delta condition [21], allowing direct boundary condition enforcement while preserving the mesh-free advantages of EFG. In this study, MEFG is applied to both forward and inverse EIT problems, improving accuracy over FE and EFG, especially in complex geometries.

Furthermore, recognizing the gap between simulated and measured data due to system noise, modeling errors, and uncertainties, a neural network-based correction using Back-Propagation (BP) is introduced to better approximate this nonlinear relationship. The neural network serves as a data-driven correction mechanism, further improving inversion accuracy and robustness.

2. Formulation of theforward problem

The forward problem in EIT models the relationship between the internal resistivity distribution and the resulting voltage data on the boundary, governed by an electromagnetic formulation.

The forward problem can be stated as follows:

Given the geometry of the domain, the distribution of electrical conductivity (or resistivity) within the region, and the configuration of current injection and electrode placement, compute the resulting electrical potential on the boundary.

Fig. 1. shows a 2D conducting region Ω with electrical resistivity ρ(x), and L electrodes positioned on the boundary ∂Ω. Each adjacent electrode pair defines a port through which electric currents are injected.

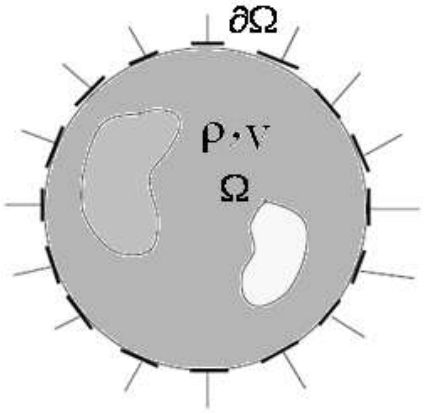

Fig.1. Conducting region Ω with electrical resistivityρ and locations of the electrodes.

The current source is applied to one port, and the voltage difference at the other ports is measured. For each current injection, the resulting electric potential distribution u(x) is generated throughout the domain.

To construct a complete dataset, the current source is sequentially applied to each port while voltage measurements are recorded from the remaining ports. The number of independent voltage measurements that can be collected from a system with L electrodes is $L(L-3)/2$ [22].

2.1.Governing equations

In the case of a linear, isotropic, and quasi-static medium, the electric potential field u(x) within the domain is governed by Laplace's equation:

$$\nabla.\sigma\nabla u = \nabla.\rho^{-1}\nabla u = 0 \qquad (1)$$

where σ is the electrical conductivity, ρ is the electrical resistivity, and u is the electric scalar potential. Assuming the current source exits from the electrode k

and enter to electrode l, the boundary condition can be shown as [23]:

$$u = 0 \quad \text{at electrode k}, \quad k = 1, 2, \ldots, L$$
$$(\text{Dirichlet boundary condition}(\partial\Omega_D))$$

$$\sigma \frac{\partial u}{\partial n} = \begin{cases} J_l & \text{at electrode } 1,\ l = 1, 2, \ldots, L \\ 0 & \text{elsewhere} \end{cases} \quad (2)$$
$$(\text{Neumann boundary condition}(\partial\Omega_N))$$

where J_l is injected current density and n is the unit vector normal to the surface.

To solve the forward model given by equation (1), the MEFG is applied and the results are validated using the standard FE method. The following sections present a detailed explanation of both FE and the Meshless MEFG method and their implementation in the EIT forward problem.

2.2. Finite Element Method

In the FE method, the solution domain Ω is discretized into Ne triangular elements and contains N_{FE} nodes. The electric potential u(x) at any point x∈Ω is approximated using a linear interpolation of nodal values as follows [24]:

$$u(\mathbf{x}) = \sum_{i=1}^{N_{FE}} \Phi_i^{FE}(\mathbf{x}) V_i \quad \forall \mathbf{x} \in \Omega \quad (3)$$

where $\mathbf{x}$ is a variable that represents the point (x, y) in the plane of the region Ω, $\Phi_i^{FE}(\mathbf{x})$, $(i = 1:N)$ are linear nodal shape functions. These shape functions are piecewise polynomial over the elements and have the selectivity property i.e. $\Phi_j^{FE}(X_i) = \delta_{ij}$; Therefore, the essential boundary conditions for $\partial\Omega$ can be directly enforced.

Formulating the system of equations by Galerkin method, a matrix form for Laplace equation can be obtained as [24]:

$$\mathbf{K}^{FE}\mathbf{V} = \mathbf{f}^{FE} \quad (4)$$

where

$$K_{i,j}^{FE} = \int_{\Omega} \rho^{-1} \nabla\Phi_i^{FE} . \nabla\Phi_j^{FE} d\Omega \quad (5)$$

$$f_i^{FE} = \int_{\partial\Omega_N} J_l \Phi_i^{FE} d\Gamma \quad (6)$$

This formulation provides the basis for solving the forward problem in EIT using FE method.

2.3. Modified Element-Free alerkinmethod (MEFG)

In the Modified Element-Free Galerkin Method, the first step is to define a set of nodal points within the domain Ω. Then the shape function for the MEFG method can be obtained by means of the Moving Least Squares (MLS) approximation method[25]. In MLS approximation $u(\mathbf{x})$ can be approximated as:

$$u(\mathbf{x}) = \sum_{j=0}^{m} p_j(\mathbf{x}) a_j(\mathbf{x}) = p^T(\mathbf{x}) a(\mathbf{x}) \quad (7)$$

where $p(\mathbf{x})$ is the monomial of order m and $a_j(\mathbf{x})$ is the non-constant coefficient which can be obtained by minimizing the following weighted quadratic functional $J(\mathbf{x}, \mathbf{a}(\mathbf{x}))$ with respect to $a(\mathbf{x})$:

$$J(\mathbf{x}, a(\mathbf{x})) = \sum_{i=1}^{n} W(\mathbf{x} - \mathbf{x}_i)[p^T(\mathbf{x}_i)\, a(\mathbf{x}) - V_i]^2 \quad (8)$$

where $w(\mathbf{x} - \mathbf{x}_i)$ is the weight function related to the node $\mathbf{x}$, and $\mathbf{x}_i$ is a node in the support domain of $\mathbf{x}$ for which $w(\mathbf{x} - \mathbf{x}_i) \neq 0$. To minimise (8), $\frac{\partial J}{\partial \mathbf{a}} = 0$ is taken and considering (8), one obtains :

$$A(\mathbf{x}) a(\mathbf{x}) = B(\mathbf{x}) V \quad (9)$$

where:

$$A(\mathbf{x})=\sum_{i=1}^{n}W(\mathbf{x}-\mathbf{x}_i)p(\mathbf{x}_i)p^T(\mathbf{x}_i) \quad (10)$$

$$B(\mathbf{x})=\left[W(\mathbf{x}-\mathbf{x}_1)p(\mathbf{x}_1),\ldots,W(\mathbf{x}-\mathbf{x}_N)p(\mathbf{x}_N)\right] \quad (11)$$

$$\mathrm{V}=\left(\mathrm{V}_1,\mathrm{V}_2,\ldots,\mathrm{V}_\mathrm{N}\right)^\mathrm{T} \quad (12)$$

Solving (9) for $a(\mathbf{x})$ and replacing it into (7), the following equation is obtained

$$u(\mathbf{x})=\mathbf{p}^T(\mathbf{x})\mathbf{A}(\mathbf{x})^{-1}\mathbf{B}(\mathbf{x})\mathbf{V}=\Phi^{EFG}(\mathbf{x})\mathbf{V} \quad (13)$$

where $\mathbf{A}(\mathbf{x})^{-1}$ is computed as [26]. Expanding (13), $u(\mathbf{x})$ can be expressed as:

$$u(\mathbf{x})=\sum_{i=1}^{N}\Phi_i^{EFG}(\mathbf{x})V_i \quad \forall\mathbf{x}\in\Omega \quad (14)$$

where the shape function $\Phi_i^{EFG}(\mathbf{x})$ is given as:

$$\Phi_i^{EFG}(\mathbf{x})=\mathbf{p}^T(\mathbf{x})\mathbf{A}^{-1}(\mathbf{x})\mathbf{B}_i(\mathbf{x}) \quad (15)$$

where $\mathbf{B}_i(\mathbf{x})$ is the i-th column of the matrix $\mathbf{B}(\mathbf{x})$.

The partial derivatives of $\Phi_i^{EFG}(\mathbf{x})$ are given by:

$$\Phi_{i,s}^{EFG}=\mathbf{p}^T{}_{,s}\,\mathbf{A}^{-1}\mathbf{B}_i+\mathbf{p}^T(\mathbf{A}^{-1})_{,s}\mathbf{B}_i+\mathbf{p}^T\mathbf{A}^{-1}\mathbf{B}_{i,s} \quad (16)$$

where Srepresents the space variable *x* or *y*, and the comma indicates the partial derivative with regard to the spatial coordinate that follows.

From Eq. (15), we can see that the performance of the MLS approximation is governed by the basis function and the weight function.

In the MLS method of this paper, the 2D linear basis function is $\mathbf{p}^T(\mathbf{x})=[1 \quad x \quad y]$ such that $m=3$, and the following tensor product weights with the cubic spline weight function is used. The tensor product weight function at any given point is given by $W(\mathbf{x}-\mathbf{x}_i)=w(r_x).w(r_y)=w_x.w_y$

where $w(r)(r=r_x \; or \; r=r_y)$ is given by:

$$w(r)=\begin{cases}\frac{2}{3}-4r^2+4r^3 & for\ r\le\frac{1}{2}\\ \frac{4}{3}-4r+4r^2-\frac{4}{3}r^3 & for\ \frac{1}{2}<r<1\\ 0 & for\ r>1\end{cases} \quad (17)$$

where $r=r_x=\left|x-x_i\right|/d_{mx}$ or $r=r_y=\left|y-y_i\right|/d_{my}$ in which $d_{mx}=d_{\max}.c_{xi}$ and $d_{my}=d_{\max}.c_{yi}$ are the size of the domain of influence of the i^{th} node in each directions. $d_{\max}$ is a scaling parameter which is typically 2-4 for a static analysis and the distance c_i is determined by searching for enough neighbor nodes for $\mathbf{A}$ to be regular, i.e. invertible [9].

Incorporating $\mathbf{x}=\mathbf{x}_k$ back in (14), we have:

$$u(\mathbf{x}_k)=\sum_{i=1}^{N}\Phi_i^{EFG}(\mathbf{x}_k)V_i=(\Phi_k^{EFG})^TV \quad (18)$$

where V represents the generalized electrical potential and $\Phi_k^{EFG}=[\phi_1^{EFG}(\mathbf{x}_k),\phi_2^{EFG}(\mathbf{x}_k),\ldots,\phi_N^{EFG}(\mathbf{x}_k)]^T$.

Then (18) can be written as matrix form as:

$$\hat{\mathbf{V}}=\mathbf{\Lambda}^\mathbf{T}\mathbf{V} \quad (19)$$

where $\hat{\mathbf{V}}$ is the nodal electrical potential, and Λ is referred to as full transformation matrix. They can be expressed as:

$$\hat{\mathbf{V}}=[V(\mathbf{x}_1),\mathrm{V}(\mathbf{x}_2),\ldots,V(\mathbf{x}_N)]^T \quad (20)$$

$$\mathbf{\Lambda}=\begin{bmatrix}\Phi_1^{EFG}(\mathbf{x}_1) & \Phi_1^{EFG}(\mathbf{x}_2) & \ldots & \Phi_1^{EFG}(\mathbf{x}_N)\\ \Phi_2^{EFG}(\mathbf{x}_1) & \Phi_2^{EFG}(\mathbf{x}_2) & \ldots & \Phi_2^{EFG}(\mathbf{x}_N)\\ \vdots & \vdots & \ddots & \vdots\\ \Phi_N^{EFG}(\mathbf{x}_1) & \Phi_N^{EFG}(\mathbf{x}_2) & \ldots & \Phi_N^{EFG}(\mathbf{x}_N)\end{bmatrix} \quad (21)$$

The generalized electrical potential can be obtained from (19):

$$\mathbf{V}=(\mathbf{\Lambda}^\mathbf{T})^{-\mathbf{1}}\hat{\mathbf{V}} \quad (22)$$

and

$$V_i=\sum_{l=1}^{N}(\Phi_l^{EFG}(\mathbf{x_i})^{-1})\hat{\mathbf{V}}_\mathbf{l} \quad (23)$$

substituting (23) in (14), we have:

$$u(\mathbf{x}) = \sum_{i=1}^{N} \Phi_i^{EFG}(\mathbf{x}) \sum_{l=1}^{N} \Phi_l^{EFG}(\mathbf{x}_I)^{-1} \hat{\mathbf{V}}_l = \sum_{l=1}^{N} \Phi_l^{MEFG}(\mathbf{x}) \hat{V}_l = \Phi^{MEFG}(\mathbf{x}) \hat{\mathbf{V}} \quad (24)$$

where $\Phi_l^{MEFG}(\mathbf{x}) = \sum_{i=1}^{N} \Phi_i^{EFG}(\mathbf{x}) \Phi_l^{EFG}(\mathbf{x}_i)^{-1}$ is called modified MLS shape function, and it satisfies the Kronecker delta function property:

$$\Phi_l^{MEFG}(\mathbf{x}_k) = \sum_{i=1}^{N} \Phi_i^{EFG}(\mathbf{x}) \Phi_l^{EFG}(\mathbf{x}_i)^{-1} = \delta_{lk} \quad (25)$$

Formulating the system of equations by Galerkin method, a matrix form for Laplace equation can be obtained as:

$$\mathbf{K}^{\mathbf{MEFG}} \mathbf{V} = \mathbf{f}^{\mathbf{MEFG}} \quad (26)$$

where

$$K_{i,j}^{MEFG} = \int_{\Omega} \rho^{-1} \nabla \Phi_i^{MEFG} . \nabla \Phi_j^{MEFG} d\Omega \quad (27)$$

$$f_i^{MEFG} = \int_{\partial \Omega_N} J_l \Phi_i^{MEFG} d\Gamma \quad (28)$$

This formulation ensures that both the accuracy and flexibility of meshless methods are retained, while essential boundary conditions can be imposed as easily as in finite element methods.

3. Neural Network based forward model correction

In this section, the Backpropagation (BP) neural network is employed to establish a relationship between the measured data obtained from a practical EIT system and the simulated outputs estimated by the numerical forward solvers described earlier.

Ideally, if the modeling and numerical solution of the forward problem in Electrical Impedance Tomography (EIT) were perfectly accurate, the forward simulation outputs and the measured data should be identical. However, due to issues such as system instability, coupling errors, and unit mismatches between theoretical modeling and experimental data, a nonlinear relationship often exists between the two. The precise nature of this nonlinear function is not required—this relationship can be treated as a "black box" that transforms theoretical data into data approximating that of the experimental system.

The BP neural network is an effective tool for modeling this black box. It is trained to learn the mapping from the numerically simulated forward problem results to the experimentally measured voltages, thereby improving the accuracy and reliability of the forward data used in EIT image reconstruction.

4. Inverse problem and NOSER algorithm

The NOSER algorithm has been developed to address the inverse problem in Electrical Impedance Tomography (EIT). In this method, the imaging domain is first divided into *n* pixels, and an initial guess is made for the conductivity distribution σ (or equivalently, the resistivity ρ within these pixels.

Electrical current patterns are applied to the electrodes, and the corresponding electrode voltages V are measured. On the other hand, using the initial guess for ρ, simulated electrode voltages U(ρ) can be computed through the forward problem. The goal is to minimize the sum of squared differences between the measured and simulated voltages, defined by the error function:

$$E(\rho) = \sum_{k=1}^{L-1} \|V^k - U^k(\rho)\|^2 = \sum_{k=1}^{L-1}\sum_{l=1}^{L}(V_l^k - U_l^k(\rho))^2 = \sum_{i=1}^{M}(V_i - U_i(\rho))^2 \quad (29)$$

where $\|\cdot\|$ denotes the L²-norm and M is the total number of measurements. Minimizing E(ρ) corresponds to solving the equation:

$$F_n(\boldsymbol{\rho}) = \frac{\partial E(\boldsymbol{\rho})}{\partial \rho_n} = -2\sum_{k=1}^{L-1}\sum_{l=1}^{L}(V_l^k - U_l^k(\boldsymbol{\rho}))\frac{\partial U_l^k(\boldsymbol{\rho})}{\partial \rho_n} \quad (30)$$

Using Newton's method, the solution is updated iteratively. The resulting system of equations can be written as:

$$\boldsymbol{\rho}_{new} = \boldsymbol{\rho}_{old} - J_F^{-1}(\boldsymbol{\rho}_{old})F(\boldsymbol{\rho}_{old}) \quad (31)$$

where:

$$J_F(\boldsymbol{\rho}) = A_{n,m} + \mu A_{n,m}\delta_{n,m} \quad (32)$$

$$A_{n,m} = 2\sum_{k=1}^{L-1}\sum_{l=1}^{L}\frac{\partial U_l^k}{\partial \rho_n}\frac{\partial U_l^k}{\partial \rho_m} \quad (33)$$

The Jacobian $\frac{\partial \mathbf{U}^k(\boldsymbol{\rho}_{old})}{\partial \rho_n}$ can be computed using sensitivity theorem[22] and the fast integration technique introduced in [27].

5. Forward problem simulation results

To evaluate the numerical performance of the Modified Element-Free Galerkin (MEFG) method in solving the EIT forward problem, a benchmark test was conducted. Although the geometry in this study is fixed, the proposed method is readily extendable to more complex and deformable biomedical domains. The test scenario is adapted from the setup described in [28].

Fig.2 illustrates the two-dimensional heterogeneous square domain (Ω) containing a rectangular inhomogeneity (Ω′). Sixteen electrodes of equal length are uniformly distributed along the boundary. A constant current is injected through electrode 1, and the resulting voltages are measured at the remaining electrodes.To simulate the forward problem, both FE and MEFG methods were implemented.

Fig. 3 shows the discretization approach for each solver.

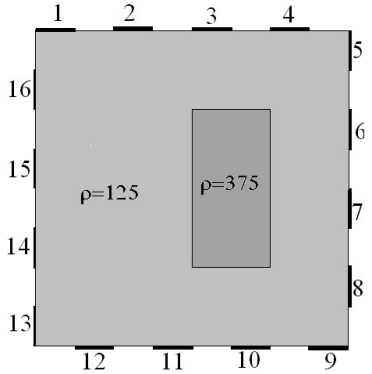

Fig.2. Test model withbackground and inhomogeneityresistivities.Electrode locations are also shown.

The FE model employs a mesh of 229 nodes and 392 triangular elements. In contrast, the MEFG model uses the same set of 229 nodes without meshing, aligning with the FE node locations.

To assess the accuracy of the solutions, the computed voltages were compared against a reference solution obtained from

a highly refined FE model comprising 100,352 elements and 50,689 nodes.

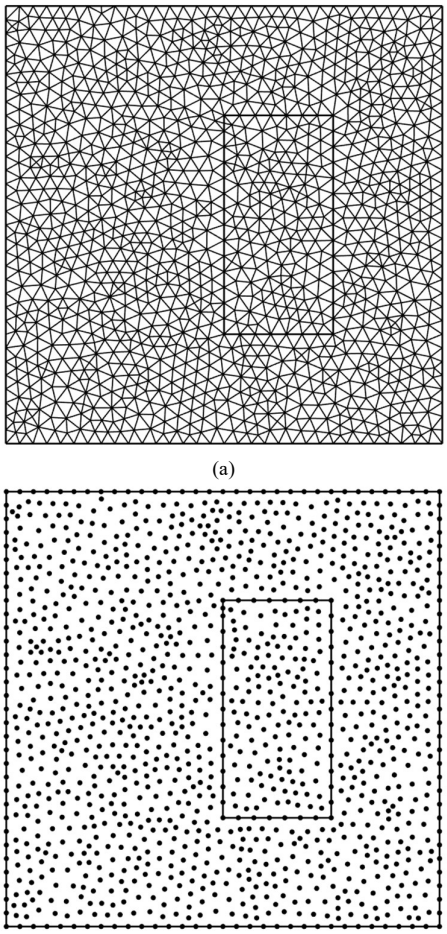

(a)

(b)

Fig.3.(a) Triangular mesh used in the FE method; (b) Node distribution used in MEFG method

The evaluation metric is the Relative Error (RE1), defined as:

$$\mathrm{RE1} = 100 \times \frac{|u - \tilde{u}|}{u} \qquad (34)$$

where $\tilde{u}$ is the electrode's potential predicted by the forward model, and u is the exact electrode's voltages.

Table 1 presents the computed electrode voltages and their associated RE1 for both FE and MEFG methods. Table 2 provides a comparison of the mean RE1 across all electrodes.

The results clearly demonstrate that the MEFG method yields improved accuracy compared to the traditional FE. As shown in Table 2, MEFG reduces the mean RE by approximately 22% relative to FE, while maintaining the same number of computational nodes.

Table 1. Voltage values and Relative Errors (RE1%) for each method per electrode

Electrode	Analytical	FE		MEFG	
		Solution	RE1 %	Solution	RE1%
1	-7.27	-6.93	4.74	-7.16	1.60
2	- 1.36	-1.30	4.37	- 1.33	1.89
3	-2.14	- 2.01	5.83	-2.02	5.46
4	-3.17	-2.98	5.98	-3.04	3.96
5	-2.23	-2.09	6.23	-2.13	4.38
6	-0.71	-0.67	5.28	-0.67	5.29
7	-1.32	-1.24	6.29	-1.26	4.97
8	-2.32	-2.17	6.22	-2.20	4.93
9	-1.96	-1.84	6.12	-1.87	4.54
10	-0.73	-0.70	4.29	-0.71	2.65
11	-1.86	-1.77	4.70	-1.78	3.99
12	-7.33	-7.00	4.497	-7.00	4.52
13	-33.15	-31.75	4.23	-32.63	1.57
14	-6.33	-6.34	0.09	- 6.13	3.26
15	-7.41	-7.21	2.77	-7.24	2.38
16	-9.13	-8.79	3.72	-8.83	3.20

These findings highlight the effectiveness of MEFG in enhancing forward model fidelity in EIT without the need for mesh generation. This is particularly advantageous in applications involving irregular or deformable geometries where mesh generation is complex or unstable.

Table 2. Mean Relative Errors for each forward solver method

Method	Number of Nodes	Mean RE(%)
FE	229	4.71
MEFG	229	3.66

6. Inverse problem simulation results

To evaluate the effectiveness of the MEFG in solving the inverse problem of EIT, we reconstructed conductivity images using both MEFG and FE as forward solvers. The benchmark test is conducted on the rectangular domain with a known inhomogeneity to assess the accuracy and efficiency of image reconstruction.

To quantify the accuracy of numerical results, the following mean relative error RE_2 have been used in the inverse problem:

$$RE_2 = \frac{\sqrt{(\boldsymbol{\rho}^{cal}-\boldsymbol{\rho}^{true})(\boldsymbol{\rho}^{cal}-\boldsymbol{\rho}^{true})^T}}{\sqrt{\boldsymbol{\rho}^{true}\boldsymbol{\rho}^{true^T}}}\times 100\% \quad (35)$$

Where $\boldsymbol{\rho}^{cal}$ is the calculated resistivity vector, and $\boldsymbol{\rho}^{true}$ is the actual resistivity vector.

In the MEFG, the forward problem is solved using an irregular distribution of 350 nodes, while the FE model utilizes a structured mesh with 357 nodes and 648 elements. For image reconstruction, a 16×16pixel grid (256 pixels) is used to compute the Jacobian matrix. To avoid the inverse crime, the simulated measurement data were generated using a high-resolution FE model consisting of 100,352 elements and 50,689 nodes, ensuring no correlation between simulation and reconstruction domains.

To enhance the accuracy of forward solutions in each iteration, a Backpropagation Neural Network is trained to map simulated voltages to their corresponding high-fidelity reference values. A training dataset consisting of 100 samples generated from various resistivity distributions is used for this purpose. The neural network is trained using the Levenberg–Marquardt optimization algorithm, achieving good convergence and effectively minimizing the gap between simulated and exact data.Fig. 4 demonstrates the neural network's performance before and after training, showing improved alignment between simulated and actual voltages. This data correction contributes to higher image fidelity in the inverse problem. Reconstructed images for both FE and MEFG forward solvers are shown in Fig. 5. Visual inspection reveals that both methods can localize the inhomogeneity; however, MEFG provides slightly sharper boundaries and more accurate contrast.

Quantitative comparisons of performance are presented in Table 3, which lists the RE2% and execution time for each method. Although MEFG incurs slightly more computational time due to its meshless nature and integration procedures, it provides a marginally better reconstruction accuracy (RE = 23.87%) compared to FE (RE = 25.07%).

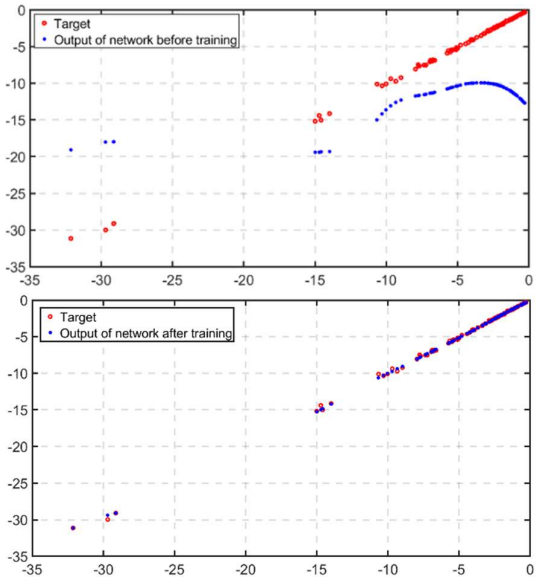

Fig.4. Relationship between exact data and neural network output before and after training.

These results confirm the capability of MEFG as a reliable alternative to FE for EIT image reconstruction, particularly when dealing with irregular or deforming geometries where mesh generation is problematic.

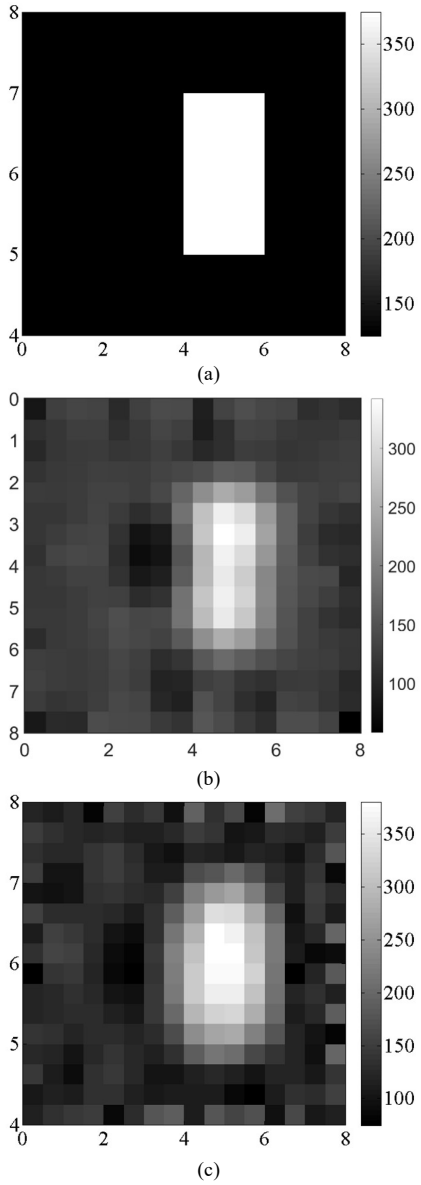

Fig.5. (a) Ground truth image. Reconstructed images using the Noser method with (b) FE and (c) MEFG forward solvers.

Table 3: Comparison of the performances of the MEFG with the FE in the inverse problem

Forward solver	RE%	Execution time (Sec.)
MEFG	23.87	94.59
FE	25.07	72.06

7. Impact of measurement noise

In the previous section, the simulated data used to solve the inverse problem were noise-free. In this section, we investigate the impact of random noise on the quality of image reconstruction using the same test model. To this end, noisy measurement data are generated by adding normally distributed noise to the high-fidelity simulated data produced by a refined FE model.The noisy data V_{noisy} are generated according to the following equation [29]:

$$V_{noisy} = V + \tilde{N}(0,1) \times [V_{\max} - V_{\min}] \times X$$

where V is the noise-free simulated voltage, V_{max} and V_{min} are the maximum and minimum values of the simulated voltage data,$X$is the noise percentage, and $\tilde{N}(0,1)$ is a normally distributed random variable with zero mean and unit standard deviation, normalized to the range of the voltage data.

Noisy data were created for different levels of random noise, ranging from 0.01% to 1%. The reconstruction error, denoted as RE2%, was calculated using both the FE and MEFG forward solvers to assess the robustness of each method under noise contamination. Table 4 presents the results. As shown in Table 4, both methods exhibit increased reconstruction error as the noise level increases. However, the MEFG forward solver demonstrates

greater robustness to noise. While the FE-based reconstruction becomes significantly less reliable with even moderate noise (e.g., 85.06% error at 0.5% noise), the MEFG method maintains a more gradual increase in error (40.85% at the same noise level). Beyond 1% noise, both methods become unstable.

Table 4. Reconstruction error (RE2%) for different levels of added noise using FE and MEFG forward solvers

Noise Level (%)	RE_2%	
	MEFG	FE
0.00	23.87	25.07
0.01	24.02	25.31
0.05	24.07	25.69
0.10	25.68	29.03
0.50	40.85	85.06
1.00	Unstable	Unstable

8. Conclusion

This study introduced a Modified Element-Free Galerkin Method for solving the forward and inverse problems in Electrical Impedance Tomography. By incorporating shape functions with the Kronecker delta property, the MEFG retains the mesh-free nature of traditional EFG while enabling accurate and direct imposition of boundary conditions. Numerical results confirm that the MEFG enhances forward modeling accuracy compared to conventional finite element methods. Furthermore, integrating a back-propagation neural network into the inverse problem improves image reconstruction and the stability and accuracy of the meshless MEFG approach in noisy environments is asseeed, showing it more suitable for practical applications of EIT where measurement noise is inevitable. These findings demonstrate the potential of the M approach as a robust and accurate tool for practical biomedical EIT applications.

References

[1] S. Mansouri, Y. Alharbi, F. Haddad, S. Chabcoub, A. Alshrouf, and A. A. Abd-Elghany, "Electrical impedance tomography–recent applications and developments," J. Electr. Bioimpedance, vol. 12, no. 1, p. 50, 2021.

[2] Y. Li, N. Wang, L. F. Fan, P. F. Zhao, J. H. Li, L. Huang, and Z. Y. Wang, "Robust electrical impedance tomography for biological application: A mini review," Heliyon, vol. 9, no. 4, p. e15291, 2023.

[3] B. Brazey, Y. Haddab, and N. Zemiti, "Robust imaging using electrical impedance tomography: Review of current tools," Proc. R. Soc. A: Math. Phys. Eng. Sci., vol. 478, no. 2258, p. 20210713, 2022.

[4] Y. Shi, Z. Yang, F. Xie, S. Ren, and S. Xu, "The research progress of electrical impedance tomography for lung monitoring," Front. Bioeng. Biotechnol., vol. 9, p. 726652, 2021.

[5] G. Franchineau, A. H. Jonkman, L. Piquilloud, T. Yoshida, E. Costa, H. Rozé, and M. Schmidt, "Electrical impedance tomography to monitor hypoxemic respiratory failure," Am. J. Respir. Crit. Care Med., vol. 209, no. 6, pp. 670–682, 2024.

[6] A. Adler, "Electrical impedance tomography," in Electrical Impedance Tomography, A. Adler, Ed., Boca Raton, FL: CRC Press, 2021, pp. 3–11.

[7] L. Zhou, B. Harrach, and J. K. Seo, "Monotonicity-based electrical impedance tomography for lung imaging," Inverse Problems, vol. 34, no. 4, p. 045005, 2018.

[8] Y. Li, L. Rao, R. He, G. Xu, Q. Wu, W. Yan, G. Dong, and Q. Yang, "A novel combination method of electrical impedance tomography, inverse problem for brain imaging," IEEE Trans. Magn., vol.41, no.5, pp.1848–1851, 2005.

[9] M. Mhajna and S. Abboud, "Assessment of cardiac stroke volume in patients with implanted cardiac pacemaker using parametric electrical impedance tomography: A theoretical

2D study," Int. J. Numer. Methods Eng., vol. 29, pp. 630–640, 2013.

[10] S. Zhang, G. Xu, X. Zhang, B. Zhang, H. Wang, Y. Xu, N. Yin, Y. Li, and W. Yan, "Computation of a 3-D model for lung imaging with electrical impedance tomography," IEEE Trans. Magn., vol. 48, no. 2, pp. 651–654, 2012.

[11] A. M. CC, R. R. De Santis Santiago, R. Di Fenza, L. E. Gibson, P. A. Restrepo, M. G. Chang, and L. Berra, "Bedside monitoring of lung perfusion by electrical impedance tomography in the time of COVID-19," Br. J. Anaesth., 2020.

[12] Y. Fu, R. Zou, S. Wang, J. Wen, L. Rong, M. Tang, and A. Adler, "Monitoring bronchoalveolar lavage with electrical impedance tomography: First experience in a patient with COVID-19," Physiol. Meas., vol. 41, no. 8, p. 085008, 2020.

[13] F. Perier, S. Tuffet, T. Maraffi, G. Alcala, M. Victor, A. F. Haudebourg, and A. M. Dessap, "Electrical impedance tomography to titrate positive end-expiratory pressure in COVID-19 acute respiratory distress syndrome," Crit. Care, vol. 24, no. 1, pp. 1–9, 2020.

[14] T. Mauri, E. Spinelli, E. Scotti, G. Colussi, M. C. Basile, S. Crotti, and A. Pesenti, "Potential for lung recruitment and ventilation-perfusion mismatch in patients with the acute respiratory distress syndrome from coronavirus disease 2019," Crit. Care Med., 2020.

[15] P. Van der Zee, P. Somhorst, H. Endeman, and D. Gommers, "Electrical impedance tomography for positive end-expiratory pressure titration in COVID-19 related ARDS," Am. J. Respir. Crit. Care Med., 2020.

[16] Z. Zhao, W. H. Kung, H. T. Chang, Y. L. Hsu, and I. Frerichs, "COVID-19 pneumonia: Phenotype assessment requires bedside tools," Crit. Care, vol. 24, no. 1, pp. 1–3, 2020.

[17] M. Šterk and R. Trobec, "Meshless solution of a diffusion equation with parameter optimization and error analysis," Eng. Anal. Bound. Elem., vol. 32, pp. 567–577, 2008.

[18] A. K. Khambampati, Y. G. Lee, K. Y. Kim, D. W. Jerng, and S. Kim, "A meshless improved boundary distributed source method for two-phase flow monitoring using electrical resistance tomography," Eng. Anal. Bound. Elem., vol. 52, pp. 1–15, 2015.

[19] A. K. Khambampati, R. L. Wang, B. S. Kim, K. Y. Kim, Y. G. Lee, and S. Kim, "A mesh-less method to solve electrical resistance tomography forward problem using singular boundary distributed source method," Flow Meas. Instrum., vol. 46, pp. 303–311, 2015.

[20] M. Hadinia and R. Jafari, "An element-free Galerkin forward solver for the complete-electrode model in electrical impedance tomography," Flow Meas. Instrum., vol. 45, pp. 68–74, 2015.

[21] C. Qin, J. Tian, X. Yang, K. Liu, G. Yan, J. Feng, and M. Xu, "Galerkin-based meshless methods for photon transport in the biological tissue," Opt. Express, vol. 16, no. 25, pp. 20317–20333, 2008.

[22] B. Brandstätter, "Jacobian calculation for electrical impedance tomography based on the reciprocity principle," IEEE Trans. Magn., vol. 39, no. 3, pp. 1309–1312, 2003.

[23] H. Razmjoo, M. Movahhedi, and A. Hakimi, "Modification on a fast meshless method for electromagnetic field computations," IET Sci. Meas. Technol., vol.5, no.5, pp.175–182, 2011.

[24] M. Vauhkonen, Electrical impedance tomography and prior information, Ph.D. dissertation, Kuopio Univ., 1997.

[25] D. Hegen, "Element-free Galerkin methods in combination with finite element approaches," Comput. Methods Appl. Mech. Eng., vol. 135, no. 1–2, pp. 143–166, 1996.

[26] S. L. Ho, S. Yang, J. M. Machado, and H. C. C. Wong, "Application of a meshless method in electromagnetics," IEEE Trans. Magn., vol. 37, no. 5, pp. 3198–3202, 2002.

[27] M. Hadinia and R. Jafari, "Improvement of performance and sensitivity of 2D and 3D image reconstruction in EIT using EFG forward model," Biomed. Phys. Eng. Express, vol. 8, no. 3, p. 035011, 2022.

[28] T. J. Yorkey, J. G. Webster, and W. J. Tompkins, "Comparing reconstruction algorithms for electrical impedance tomography," IEEE Trans. Biomed. Eng., no. 11, pp. 843–852, 2007.

[29] R. Kulkarni, Analytical forward models for breast cancer detection using electrical impedance tomography, M.S. thesis, Rensselaer Polytech. Inst., 2009.